Spin transport and thermoelectric properties in chiral selenium crystals

Luz Ramírez-Montes,[1,2,*] William López-Pérez [2], A. González-García [2,3] and Rafael González-Hernández [2]

[1]*Departamento de Ciencias Naturales y Exactas, Universidad de la Costa, Barranquilla, Colombia*
[2]*Departamento de Física y Geociencias, Universidad del Norte, Km. 5 Vía Antigua Puerto Colombia, Barranquilla 080020, Colombia*
[3]*NANOlab Center of Excellence, University of Antwerp, Belgium*

Chiral materials, characterized by their nonsuperimposable mirror-image symmetry, introduce a multitude of fascinating phenomena and applications in present-day science. Here we predict the presence of the spin Hall effect (SHE) and current-induced spin polarization (CISP) within chiral selenium crystals, employing symmetry analysis and first-principles computational techniques. Notably, band structure calculations unveiled the presence of Rashba splitting, a manifestation of spin-orbit coupling, in these noninversion-symmetric materials. Moreover, our findings reveal that bulk selenium holds promise as a thermoelectric material by adjusting the carrier concentration accordingly. The ZT value we have obtained for t-Se is similar to that of the layered thermoelectric material SnSe and higher than its t-Te counterpart. The unique properties of chiral Se crystals, such as the Rashba splitting and the emergence of spin-related phenomena, together with their thermoelectric features, hold promise for potential applications of this chiral crystal in emerging technologies.

I. INTRODUCTION

Chirality refers to a physical property of asymmetry or handedness observed in crystals or objects that cannot be superimposed onto their mirror image, just like a left and right hand. Crystals with a chiral structure (chiral crystals) can induce unconventional spin accumulation when an electric current passes through them. This phenomenon is also referred to as current-induced spin polarization (CISP), which could potentially have a profound impact on the design of spintronic devices [1,2]. Moreover, the interplay between chirality and spin phenomena extends beyond CISP, encompassing chirality-induced spin selectivity (CISS), wherein electrons traversing chiral molecules or materials exhibit spin polarization only due to structural chirality [3,4]. These materials not only exhibit unconventional spin accumulation but also manifest unusual properties such as Rashba effect [5], the anomalous Hall effect [6], the spin Hall effect (SHE), spin selectivity effect [7], and remarkable thermoelectric [8], and topological properties [9], which make them suitable for next-generation technology applications.

Selenium, along with its structurally analogous counterpart tellurium, falls into the category of chiral crystals. Interestingly, its crystal structure is composed of a hexagonal array of atoms organized in an oriented spiral chain (as shown in Fig. 1) [10]. This helical stacking is connected through van der Waals interactions and introduces chirality into the structure. This means that the crystal structure cannot be superimposed on its mirror image. This lack of mirror symmetry in the three-dimensional arrangement of the selenium crystal structure is what makes it a chiral crystal [11].

Recently, Arunesh *et al.* revealed unconventional spin accumulation induced in the Te bulk by an electric current [2]. They reported that this phenomenon is intrinsically protected by the quasipersistent spin helix arising from the crystal symmetries present in chiral systems with spin-orbit coupling (SOC). In addition, Furukawa *et al.* reported that elemental Te, a nonmagnetic semiconductor, can display a minor local magnetization induced by an electrical current. This phenomenon can be attributed to the splitting of the bulk band structure, which arises from the chiral structure of trigonal tellurium [12]. While the spin Hall effect has been extensively investigated in various semiconductor materials [13,14], the exploration of this phenomenon in chiral materials has recently gained significant attention [12,15]. However, it is noteworthy that the manifestation of the spin Hall effect in Se, nonmagnetic materials, has not yet been reported. This knowledge gap underscores the need for an in-depth exploration of the spin-charge conversion in these chiral materials.

Research also shows that chiral crystals, such as selenium and tellurium, are highly anisotropic [16–18]. Their anisotropic properties are primarily associated with their chiral structure, which can have profound effects on their behavior and applications. Moreover, due to the outstanding physical, chemical, and biochemical properties of selenium [19], there has been significant research attention directed toward its application in developing selenium-based nanomaterials in diverse fields [20]. Fields such as medicine, where selenium plays a crucial role in important life processes such as the treatment of diseases and the regulation of protein synthesis [21]. Selenium's versatility extends to semiconductor components utilized in a multitude of applications, e.g., biosensors, solar cells, and electrocatalysis [22], as well as applications across thermoelectricity. Zhang *et al.* recently reported a high thermoelectric performance in bulk selenium,
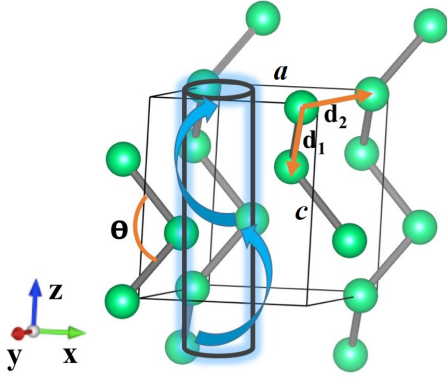
---

*ramirezlm@uninorte.edu.co

FIG. 1. Crystalline structure of bulk selenium (A8) and Se chain along the *z*-axis direction are shown. The cylinder illustrates the chiral geometry along the *z* axis. The nearest-neighbor distance (d_{1-Se}), the second-neighbor distance (d_{2-Se}), the intrachain bond angle (θ), and constant lattices *a* and *c* are depicted.

which is attributed to the unique bonding characteristics, multivalley band structures, and the confinement of phonons due to the dimensionally reduced nanostructures [10].

Even though this material has been extensively studied, experimental and theoretical studies of CISP and SHE [10,23] in bulk selenium are almost nonexistent at present. Therefore, motivated by above developments and by recent theoretical reports about the circularly polarized spin injection [2] and high-efficiency thermoelectricity found in Te semiconductor [8], here we investigate both the spin and thermoelectric transport in chiral crystals, particularly focusing on bulk selenium, a promising material for applications in emerging fields such as spintronics and thermoelectricity.

II. CALCULATION METHOD AND COMPUTATIONAL DETAILS

In order to study the properties of selenium in its trigonal A8 phase, first-principles calculations were performed using the projector-augmented wave (PAW) method [24,25], implemented in the VASP code [26,27], within the framework of density functional theory (DFT) [28,29]. To solve the Kohn-Sham equations, the generalized gradient approximation (GGA) was employed to describe the electron exchange-correlation potential, using the PBE parametrization [30]. Because the structures are arranged in trilayer configurations, held together by vdW forces, the Grimme correction was applied to describe these interactions [31]. Wave functions were expanded in plane waves up to a cutoff energy of 520 eV. We conducted structural relaxations using various approaches, including PBE, PBE+SOC, and DFT-D2 +SOC. For the optimization of structural properties, a $15\times15\times12$ *k*-point grid in the irreducible Brillouin zone within the Monkhorst-Pack special *k*-point scheme [32] was considered, while a $45\times45\times36$ *k*-point grid was used for elastic constant calculations. Afterwards, VASP, together with Phonopy [33,34], was used to calculate the total energy, ionic forces, and structural stress using a $5\times5\times5$ supercell.

As forces result from the gradients of the total energy concerning atomic positions, and stress emerges from derivatives

with respect to strain, we conducted total energy calculations and their initial derivatives, encompassing all parameters that define the crystal structure. Force and stress calculations help verify the material's stability. For phonon calculations, a $6\times6\times4$ supercell was used (comprising 432 atoms), and a $4\times4\times3$ *k*-point grid in the irreducible Brillouin zone was considered within the Monkhorst-Pack special *k*-point scheme. Once the stability of the 3D system is confirmed, thermoelectric properties are studied by solving the semiclassical Boltzmann transport equation, implemented in the BoltzTrap program [35], with a dense grid of $50\times50\times40$ *k*-point for integrating the irreducible Brillouin zone. Within this formalism, the electrical conductivity tensor as a function of energy, denoted as $\sigma_{\alpha\beta}(\varepsilon)$, is expressed as

$$\sigma_{\alpha\beta}(\varepsilon) = \frac{1}{N}\sum_{i,\mathbf{k}}\sigma_{\alpha\beta}(i,\mathbf{k})\frac{\delta(\varepsilon - \varepsilon_{i,\mathbf{k}})}{d\varepsilon}. \quad (1)$$

Here, $\sigma_{\alpha\beta}(i,\mathbf{k}) = e^2\tau_{i,\mathbf{k}}v_\alpha(i,\mathbf{k})v_\beta(i,\mathbf{k})$, N represents the number of $\mathbf{k}$ points, $v_\alpha(i,\mathbf{k})$ is the velocity operator associated with wavevector $\mathbf{k}$, and $\tau_{i,\mathbf{k}}$ stands for the relaxation time. The electrical conductivity [$\sigma_{\alpha\beta}(T;\mu)$], Seebeck coefficient ($S_{ij}$), and electronic thermal conductivity [$\kappa^0_{\alpha\beta}(T;\mu)$] can be written as [35]

$$\sigma_{\alpha\beta}(T;\mu) = \frac{1}{\Omega}\int\sigma_{\alpha\beta}(\varepsilon)d\varepsilon, \quad (2)$$

$$\nu_{\alpha\beta}(T;\mu) = \frac{1}{eT\Omega}\int\sigma_{\alpha\beta}(\varepsilon)(\varepsilon - \mu)d\varepsilon, \quad (3)$$

$$\kappa^0_{\alpha\beta}(T;\mu) = \frac{1}{e^2T\Omega}\int\sigma_{\alpha\beta}(\varepsilon)(\varepsilon - \mu)^2 d\varepsilon, \quad (4)$$

$$S_{ij} = E_i(\nabla_j T)^{-1} = (\sigma^{-1})_{\alpha i}\nu_{\alpha j}. \quad (5)$$

On the other hand, the lattice thermal conductivity of selenium was calculated using the phono3py code [33,34]. To attain this, second and third-order interatomic force constants were computed with $3\times3\times3$ and $2\times2\times2$ supercells generated by the phono3py code. For second-order interatomic forces, only simple atomic displacements are needed, while third-order forces require two atomic displacements. As two atomic displacements are necessary, there are numerous displacement configurations, which are reduced to 436 due to symmetry operations.

The linear response theory was used to find the spin conductivity and current-induced spin-polarized tensors. In order to evaluate the Kubo formula we have used an effective tight-binding Hamiltonian constructed in the maximally localized Wannier basis [36] as a postprocessing step of the DFT calculations. Conductivity tensors (symmetric and antisymmetric under time-reversal) were calculated by integrating the response functions on a dense $240\times240\times240$ *k*-mesh of the first Brillouin zone using the Wannier linear response code [37] Within this model, these contributions to the linear response of a physical observable $\hat{A}$ to an electric field are decomposed

TABLE I. Optimized lattice parameters (a and c), internal parameter (u), nearest-neighbor Se-Se distance in a chain (d_1), second-neighbor Se-Se distance in different chains (d_2), and intrachain bond angle (θ) for trigonal selenium and tellurium.

Functional	a (Å)	c (Å)	u	d_1 (Å)	d_2 (Å)	θ
			Se			
PBE	4.510	5.051	0.220	2.404	3.565	103.6
Other PBE [23]	4.519	5.050	0.219			
PBE+SOC	4.504	5.057	0.220	2.406	3.560	103.6
DFT-D2	4.255	5.106	0.233	2.417	3.361	104.1
Other DFT-D2 [23]	4.258	5.107	0.233			
DFT-D2+SOC	4.255	5.110	0.233	2.418	3.361	104.1
DFT-D2+SCAN	4.433	5.003	0.221	2.377	3.505	103.7
DFT-D2+SCAN+SOC	4.431	5.007	0.221	2.388	3.405	104.0
DFT-D3	4.185	5.125	0.238	2.430	3.300	103.9
Other DFT-D3 [38]	4.184	5.127		2.431		103.9
Exp. [39,40]	4.366	4.954	0.225	2.373	3.436	103.1
			Te			
PBE	4.514	5.957	0.269	2.892	3.507	102.0
Other PBE [41]	4.510	5.960		2.890	3.500	
PBE+SOC	4.513	5.988	0.269	2.901	3.511	102.1
DFT-D2	4.339	6.030	0.277	2.893	3.400	103.0
DFT-D2+SOC	4.336	6.064	0.277	2.901	3.404	103.2
DFT-D2+SCAN	4.260	5.971	0.284	2.890	3.323	102.2
DFT-D2+SCAN+SOC	4.257	5.996	0.284	2.897	3.324	102.4
DFT-D3	4.410	5.937	0.278	2.902	3.414	101.4
Exp. [42]	4.451	5.926	0.263	2.833	3.491	103.3

into two opposite contributions under time reversal,

$$\delta A^I = -\frac{e\hbar}{\pi}\text{Re}\sum_{\mathbf{k},m,n}\frac{\langle u_n(\mathbf{k})|\widehat{A}|u_m(\mathbf{k})\rangle\langle u_n(\mathbf{k})|\widehat{v}|u_m(\mathbf{k})\rangle\Gamma^2}{((E_F - E_n(\mathbf{k}))^2 + \Gamma^2)(E_F - E_m(\mathbf{k}))^2 + \Gamma^2)},$$

(6)

$$\delta A^{II} = -2e\hbar.\text{Im}\sum_{\mathbf{k},m\neq n}^{\substack{n \text{ occ.}\\ m \text{ unocc.}}}\frac{\langle u_n(\mathbf{k})|\widehat{A}|u_m(\mathbf{k})\langle u_n(\mathbf{k})|\widehat{v}|u_m(\mathbf{k})\rangle}{(E_n(\mathbf{k}) - E_m(\mathbf{k}))^2}.$$

(7)

Here $u_n(\mathbf{k})$ are the Bloch functions of a single band n, $\mathbf{k}$ is the Bloch wave vector, $\varepsilon_n(\mathbf{k})$ is the band energy, E_F is the Fermi energy and $\hat{v}$ is the velocity operator. Sums over $\mathbf{k}$ run over all $\mathbf{k}$ points into the first Brillouin zone.

When considering $\hat{A} = \hat{j}^s$, which represents the spin-current operator as defined by $\hat{j}_{i,j}^s = \frac{1}{2}\{\hat{s}_i, \hat{v}_j\}$, the resulting spin conductivity in Eq. (7) corresponds to the conventional intrinsic spin Hall effect (SHE). This contribution remains constant as Γ approaches zero, making it observable to nonmagnetic systems and particularly in materials with significant spin-orbit coupling. On the other hand, when $\hat{A} = \hat{s}$, indicating the spin operator, Eq. (6) represents the symmetric part of the current-induced spin-polarized (or spin accumulation) tensor, known as the Boltzmann contribution. Notably, this contribution diverges at $1/\Gamma$ when Γ tends to zero, with a constant relaxation time given by $\hbar/2\Gamma$.

III. RESULTS AND DISCUSSION

A. Structural and dynamic stability

The schematic representation of the crystal structure of trigonal selenium and tellurium is illustrated in Fig. 1, which contains three atoms at atomic positions $(u, u, 0)$,

$(0, 1 - u, 1/6)$, and $(1 - u, 0, 5/6)$. It comprises helical chains arranged in a hexagonal lattice. The space group is either P3$_1$21 (no. 152) or P3$_2$21 (no. 154), contingent upon the handedness of the screw configuration. However, despite the apparent structural disparity, these two distinct helical arrangements are geometrically equivalent, connected by spatial inversion. Consequently, their structural parameters, energy band structures and linear optical properties are anticipated to be congruent. Moreover, the nonzero elements of the second-order susceptibility tensor would be identical and are mutually interrelated. The valence electron configurations of selenium and tellurium are $4s^2 4p^4$ and $5s^2 5p^4$, respectively, meaning that one-third of the p bands remain unoccupied. Consequently, each atom forms covalent bonds with two neighboring atoms within each chain, while also interacting with four second-nearest-neighbor atoms from adjacent chains through van der Waals forces. As depicted in Fig. 1, the lattice constant a represents the distance between adjacent chains, while lattice constant c reflects the height of the unit cell along the chain direction (z axis). Notably, the internal parameter u can be correlated with lattice constant a and the helix radius. It is interesting to note that the ratio (d_2/d_1) of interchain to intrachain distances in tellurium is smaller than in selenium (Table I), suggesting a reduced level of structural anisotropy in tellurium [43].

We have optimized the structural parameters of the trigonal Se and Te in the chiral space groups P3$_1$21 and P3$_2$21, corresponding to the right-handed or left-handed screw, respectively [44–46]. The results show that the structural parameters are identical in both space groups. Table I shows the optimized values for lattice parameters a and c, internal parameter u, shortest Se-Se or Te-Te distance in a chain (d_1), shortest
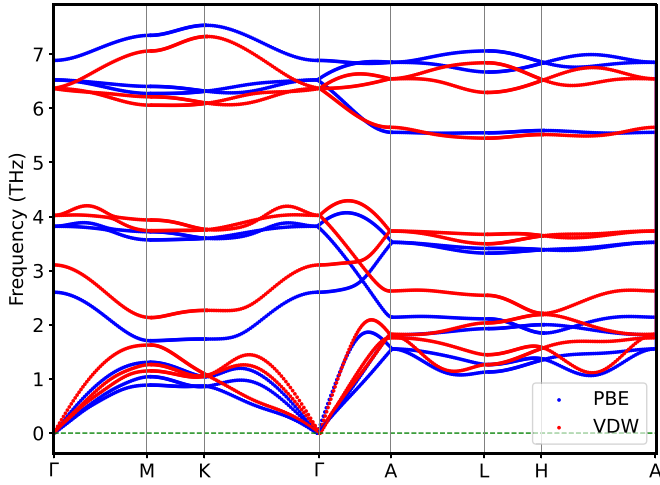
FIG. 2. Phonon dispersion relation for selenium in the A8 crystalline structure using PBE and PBE+vdW.

distance in different chains (d_2), and intrachain bond angle (θ) for trigonal selenium and tellurium. These parameters in particular have been calculated using GGA-PBE and considering additional contributions. Our GGA-PBE results for the lattice parameters (*a* and *c*) and the internal parameter (*u*) are very close to the GGA-PBE reported by other authors [23,41]. We have added the Grimme D2 correction (DFT-D2) to include van der Wals interactions. Our DFT-D2 results are similar to those reported in reference [23] for selenium. Our calculations for selenium using the Grimme D3 correction (DFT-D3) yield values very similar to those reported in other study [38]. To improve the description of weak and strong bonds, as well as the proper separation between valence electrons and atomic nuclei, we have used strongly constrained and appropriately normed (SCAN) potentials. When we include spin-orbit coupling, the structural parameters change slightly with respect to values obtained without spin-orbit coupling. Comparing with the experimental data we can see that the error for lattice constant *a* is in the range of 1.5% to 4.2%, and for parameter *c* it is between 1.0% and 3.5%. In general, the values of the structural parameters calculated with the different exchange-correlation approximation are in good agreement with the experimental data [39,40]. The experimental structural parameters and those obtained in this paper have greater value for tellurium compared to those of selenium. This may influence the difference in electronic structures of these systems. So, it is to be expected that they present different behaviors in several of their properties. All the properties calculated and presented in this paper have been obtained using the lattice parameters optimized with DFT-D2+SOC.

Figure 2 depicts the phonon dispersion relations along high-symmetry *k* points with PBE and PBE+vdW interactions. The incorporation of DFT-D2 corrections align phonon dispersion with the consensus found in the literature [23]. The absence of imaginary frequencies confirms the thermodynamic stability of the trigonal selenium structure. Our analysis reveals nine distinct phonon branches, comprised of three acoustics and six optical branches. Trigonal selenium, unlike some materials, lacks an acoustic-optical gap, leading to the overlap of low-frequency optical branches along the

L–H direction with the acoustic branches. This absence of an acoustic-optical gap enhances the acoustic-optical phonon scattering rate, a phenomenon commonly observed in materials exhibiting low thermal conductivity. Along the Γ–M direction, the optical phonon branch demonstrates relatively greater intensity compared to the H–A direction. This variation in optical phonon strength has implications for heat transport within the crystal lattice. Moreover, the slope of the acoustic phonon modes, approximating the group velocity magnitude, suggests a smaller phonon group velocity along the direction perpendicular to the chain. This observation sheds light on the anisotropic nature of phonon transport, indicating more efficient heat conduction along the chain direction.

Traditionally, optical phonons are often overlooked in thermal conductivity analyses due to their typical nearly dispersionless nature and small group velocities. However, despite their limited direct contribution to heat transport, optical phonons are an essential scattering channel for heat-carrying acoustic phonons. Our results confirm that acoustic phonons, particularly along the direction perpendicular to the chain, predominantly influence the thermal conductivity of selenium.

An intriguing phenomenon emerges when considering the direction parallel to the chain (*z* axis in Fig. 1). Contrary to the conventional expectation of minimal impact, the optical phonon branch in selenium exhibits a remarkably high contribution, particularly at room temperature. This noteworthy observation of substantial optical phonon involvement in bulk materials is seldom reported in the literature.

The unusual behavior of heightened contributions from optical phonon modes in selenium finds resonance in similar observations in chiral materials [57,58]. This parallelism across diverse materials underscores the significance of optical phonons in influencing thermal transport, challenging conventional assumptions about their limited role in bulk material heat conduction.

In order to determine parameters related to stiffness and elasticity, the mechanical response of the materials under study was analyzed. To carry out the analysis of elastic properties, the elastic constants C_{ij} were calculated using the stress-strain relationship implemented in the VASP code [26,27]. Once the C_{ij} constants are computed, elastic parameters such as bulk modulus, shear modulus, Young's modulus, and Poisson's ratio can be obtained [59].

This procedure takes advantage of the anisotropic form of Hooke's law,

$$\sigma_i = C_{ij}\epsilon_j, \tag{8}$$

where σ_i and ϵ_j are the stress and strain, respectively, C_{ij} are the elastic constants, and i, j are integers. It is often useful to express this law in matrix notation, also called Voigt notation. To do this, the symmetry of the stress and strain tensors is taken into account. For a trigonal system such as selenium or tellurium, it can be written in the form

$$
\begin{pmatrix} \sigma_1 \\ \sigma_2 \\ \sigma_3 \\ \sigma_4 \\ \sigma_5 \\ \sigma_6 \end{pmatrix} =
\begin{pmatrix}
C_{11} & C_{12} & C_{13} & C_{14} & 0 & 0 \\
C_{12} & C_{11} & C_{13} & -C_{14} & 0 & 0 \\
C_{13} & C_{13} & C_{33} & 0 & 0 & 0 \\
C_{14} & -C_{14} & 0 & C_{44} & 0 & 0 \\
0 & 0 & 0 & 0 & C_{44} & C_{14} \\
0 & 0 & 0 & 0 & C_{14} & C_{66}
\end{pmatrix}
\begin{pmatrix} \epsilon_1 \\ \epsilon_2 \\ \epsilon_3 \\ \epsilon_4 \\ \epsilon_5 \\ \epsilon_6 \end{pmatrix}.
$$

TABLE II. Elastic moduli: bulk modulus [B (GPa)], shear modulus [G (GPa)], Young's modulus [Y (GPa)], and Poisson's ratio (v) for selenium and tellurium. Our results using van der Waals correction are compared with other experimental and theoretical values.

Elastic moduli	Se	Se (Exp) [47]	Se (Other) [10]	Te	Te (Exp) [47]
B (GPa)	13.86	11.06		25.87	19.00
B_v (GPa)	20.00			28.32	
B_R (GPa)	7.72			23.42	
G (GPa)	8.73		9.50	18.44	17.00
G_v (GPa)	13.46			23.57	
G_R (GPa)	4.00			13.30	
Y (GPa)	21.64		23.40	44.69	41.00
v	0.24	0.33	0.23	0.21	0.22

In this symmetry it is true that $C_{22} = C_{11}$, $C_{55} = C_{44}$ and $C_{66} = (C_{11}-C_{12})/2$. The independent constants considered in the stress-strain relationship are C_{11}, C_{12}, C_{13}, C_{14}, C_{33}, and C_{44}. All elastic moduli have been calculated using the formulas given in Ref. [60], and have been listed in Table II.

The elastic moduli are measurable quantities on a macroscopic scale and indicate the elasticity of the material. The bulk modulus represents the volume compressibility of the material, the shear modulus describes the deformation of the system under transverse forces, Young's modulus provides a measure of the system's stiffness, and Poisson's ratio is used as a measure of plasticity. These elastic moduli are obtained at the Voigt and Reuss limits, which provide upper and lower bounds for the real elastic moduli of the crystals, respectively. Table II shows that tellurium is a stiffer material than selenium but less plastic. Our results for selenium are in good agreement with theoretical [10] and experimental [47] data. The results we obtained for elastic moduli of tellurium are consistent with experimental measurements [47].

In Table III we compare the predictions of our electronic band structure results for Se with those obtained from different functionals. We can notice that our indirect band gap from PBE (PBE-SOC) agrees well with those reported with the same functional [43,48] ([48,49]), but significantly underestimates the experimental indirect band gap value [55,56]. The underestimation of the energy gap in semiconductors by the PBE exchange-correlation energy is a widely recognized issue. This is mainly due to the fact that the simple form of GGA is not sufficiently flexible to accurately reproduce both exchange-correlation energy and its charge derivative [61,62]. Our results with DFT-SCAN+SOC improves (underestimates) the band gap value obtained with PBE (experimental) by 26.9% (∼30%) [56], which is in a good agreement with the results obtained by Moustafa *et al.* [49]. The best results for the electronic band structure are displayed by the hybrid functionals. They underestimate

TABLE III. Calculated electronic band structures of pure bulk t-Se obtained from different functionals and experimentally.

| Functional	Indirect (eV)	Direct (eV)	Δ (meV)	Ground state (GS)
PBE (152)	0.989	1.200	211	Indirect
PBE (154)	0.989	1.200	211	Indirect
Other PBE [48]	0.960	1.010	50	Indirect
Other PBE [38]	0.980	1.210	230	Indirect
Other PBE [43] ($P3_121$)	1.002			Indirect
DFT-D2 (152)	0.682	0.800	118	Indirect
DFT-D2 (154)	0.682	0.800	118	Indirect
Other DFT-D2 [38]	0.720	0.800	80	Indirect
DFT-D2+SOC (152)	0.645	0.673	28	Indirect
PBE+SOC (152)	0.957	1.063	106	Indirect
Other PBE+SOC [49]	0.990	1.090	100	Indirect
Other PBE+SOC [48]	0.960	1.010	50	Indirect
DFT-SCAN+SOC (152)	1.224	1.351	127	Indirect
Other DFT-SCAN+SOC [49]	1.250	1.370	120	Indirect
HSE06 [48]	1.700	1.790	90	Indirect
HSE06-SOC [48]	1.700	1.790	90	Indirect
HSE06+SOC [49]	1.720	1.820	100	Indirect
HSE [43] ($P3_121$)	1.759			Indirect
HSE+SOC [43] ($P3_121$)	1.735			Indirect
GW+SOC [50]	1.740			Indirect
G_0W_0+SOC [49]	1.780	1.940	160	Indirect
MBJLDA+SOC [51]	1.480	1.570	90	Indirect
mBEEF+SOC [49]	1.430	1.550	120	Indirect
Exp. [52]		1.950		Direct
Exp. [53]		1.800		Direct
Exp. [54]		1.790		Direct
Exp. [55]	1.850			Indirect
Exp. [56]	1.800			Indirect
Exp. [48]		1.950		Direct
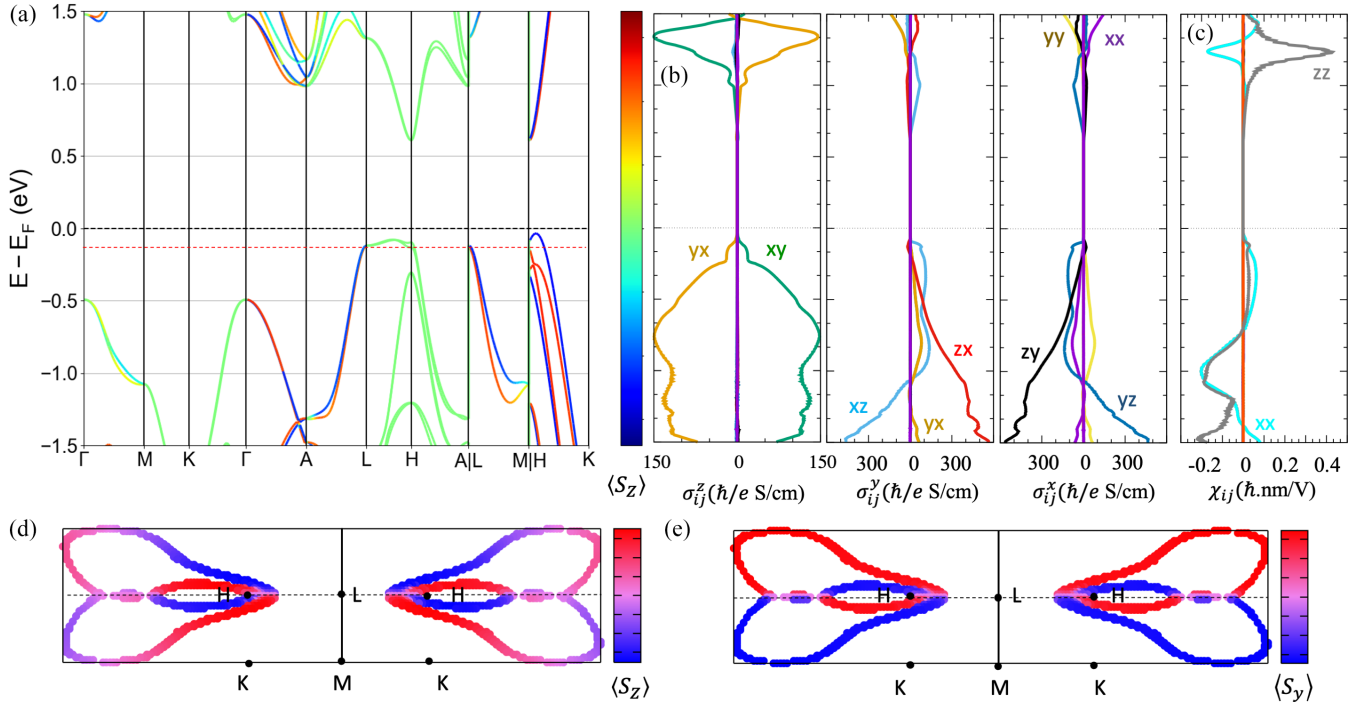
FIG. 3. (a) Electronic band structure with projected spin-z component. (b) Spin Hall conductivity tensor σ_{ij}^{spin} and (c) current-induced spin polarized χ_{ij} as a function of the Fermi level. Fermi level is located at the top of the valence band. Spin texture for (d) S_z and (e) S_y spin components in the $k_y = 0$ plane. M-K-L-H high symmetry points in the BZ are indicated. It is noted a Rashba spin splitting along the k_z axis. SOC interaction is included in the DFT calculations.

the experimental band gap by less than 6% [43,48–50]. We have also found that the electronic properties are independent of the handedness, as reported by [46]. On the other hand, there appears to be a contradiction between the band gap results obtained from density functional theory (indirect band gap) and those obtained from optical spectroscopy methods (direct band gap) [48,54,63]. This fact can be explained by the small energy difference (from ∼28 to ∼230 meV) between the indirect and direct absorption, as shown in Table III, which makes it difficult to distinguish them experimentally.

B. Spin transport properties

In Fig. 3(a), the electronic band structure of bulk Se is displayed, calculated with DFT-D2+SOC. An indirect band gap energy of approximately 0.7 eV is observed, aligning with the findings of Ertekin *et al.* [64]. Notably, the impact of SOC gives rise to a distinct phenomenon known as Rashba splitting. As illustrated in Fig. 3(a), this band spin splitting is particularly prominent along the k_z paths, specifically along the L-M and H-K directions. Noticeably, a considerable band spin splitting close to the Fermi energy is observed along the K-H high symmetry line, even in this case, where the SOC strength is relatively low. This splitting is independent of band gap value.

We have generated spin texture plots for the z and y spin components along the constant k_y plane at an energy of $E = E_f - 100$ meV, as shown in Figs. 3(d) and 3(e). These figures reveal a Rashba spin splitting aligned along the k_z axis and mainly concentrated around the $k_z = \pi$ plane, with the S_z and S_y components shown as the most significant signals.

Experimental validation of a similar phenomenon has been achieved through spin- and angle-resolved photoemission spectroscopy measurements (S-ARPES) on Te, a structural configuration equivalent to Se [65].

Rashba spin splitting, arising due to the absence of inversion symmetry in the crystal lattice, couples the electronic spin states with their momentum. This coupling leads to the emergent spin-related phenomena, including the SHE and CISP [66]. To investigate these phenomena in Se, we have employed the Kubo formula—as presented by Eqs. (4) and (5)—to calculate the spin Hall conductivity (SHC) and CISP responses as functions of the Fermi energy, as shown in Figs. 3(b) and 3(c), respectively.

It is essential to highlight that various components of the SHC tensor exhibit nonzero values, dictated by the crystal symmetry inherent to the material (space group #152). A symmetry analysis reveals that the SHC tensor possesses nontrivial components, as explained by the following matrix [67]:

$$\sigma_{ij}^x = \begin{bmatrix} \sigma_{xx}^x & 0 & 0 \\ 0 & -\sigma_{xx}^x & -\sigma_{xz}^y \\ 0 & -\sigma_{zx}^y & 0 \end{bmatrix},$$

$$\sigma_{ij}^y = \begin{bmatrix} 0 & -\sigma_{xx}^x & \sigma_{xz}^y \\ -\sigma_{xx}^x & 0 & 0 \\ \sigma_{zx}^y & 0 & 0 \end{bmatrix}.$$

$$\sigma_{ij}^z = \begin{bmatrix} 0 & -\sigma_{xy}^z & 0 \\ \sigma_{xy}^z & 0 & 0 \\ 0 & 0 & 0 \end{bmatrix}.$$

Figure 3(b) indicates a consistency between the calculated SHC components and the symmetry analysis, validating our computational results. In addition, the σ_{ij}^{x} and σ_{ij}^{y} components are more significant than σ_{ij}^{z}. Close to the Fermi energy ($E = E_f - 100$ meV), the dominant component is σ_{xz}^{y}, which suggests an enhanced spin current response with an electric field along the z axis representing the chiral axis of the Se crystal structure.

On the other hand, the Rashba spin splitting leads to the emergence of a notable phenomenon known as CISP or the inverse spin galvanic effect. CISP is characterized by the generation of spin polarization within a material when subjected to an applied electric field. In Fig. 3(c), the presence of CISP in selenium becomes evident when the Fermi energy is shifted through electron or hole doping.

For $E = E_f - 100$ meV, we observed a substantial CISP signal of approximately 0.05 $\hbar$.nm/V, which is comparable to the case of tellurium (Te), as reported in [2]. Remarkably, this value exhibits an increase as we introduce hole doping into the material, and can be controlled by employing gating techniques. To compute the CISP effect, we have used Eq. (4), with the relaxation time as is calculated in the next section. Furthermore, we verified the nonzero components of the CISP tensor through symmetry analysis, and these findings align with the results presented in Fig. 3(c),

$$\chi_{ij} = \begin{bmatrix} \chi_{xx} & 0 & 0 \\ 0 & \chi_{xx} & 0 \\ 0 & 0 & \chi_{zz} \end{bmatrix}.$$

We have found that the CISP components undergo a change of sign depending on the handedness of the crystal (see the Supplemental Material [68]). Notably, this effect vanishes when the Se crystal transforms to an achiral state (space group #166) [46]. Conversely, our findings indicate that properties such as phonon dispersion, electrical conductivity, and SHC components remain unaffected by variations in the Se crystal chirality.

SHE and CISP in chiral crystals can offer a platform for manipulating and controlling electron spins with high precision, which is essential for developing next-generation spintronic devices and exploring fundamental quantum phenomena.

C. Thermoelectric properties

Thermoelectric materials play a fundamental role in modern technology due to their ability to convert heat energy into electrical energy and vice versa, offering promising solutions for energy harvesting and efficient cooling systems [69]. Seebeck effect, which describes the generation of a voltage across a temperature gradient in a conductive material, is the core for thermoelectric devices. The efficiency of thermoelectric materials in converting heat into electricity is quantified by the figure of merit (ZT),

$$\text{ZT} = \frac{S^2 \sigma T}{(k_e + k_L)}, \tag{9}$$

where S, σ, $S^2 \sigma$, k_e, and k_L are the Seebeck coefficient, electrical conductivity, power factor, electron thermal conductivity,

TABLE IV. Elastic modulus C, constant strain potential E_1, effective mass m^*, and carrier relaxation time τ for selenium and tellurium at room temperature.

	Carrier	C (GPa)	E_1 (eV)	m^* (m_0)	τ (10^{-14} s)
Se$_{x/y}$	n-type	12.90	–8.059	0.272	4.94
Ref. [10]		12.70	–7.862	0.223	6.77
Ref. [47]		19.80			
Se$_x/y$	p-type	12.90	–10.471	0.542	1.02
Ref. [10]		12.70	–10.262	0.565	0.99
Ref. [47]		19.80			
Se$_z$	n-type	82.20	–16.417	0.116	26.80
Ref. [10]		81.22	–19.246	0.117	18.96
Ref. [47]		83.6			
Se$_z$	p-type	82.20	–11.369	0.286	14.40
Ref. [10]		81.22	–9.606	0.280	20.60
Ref. [47]		83.6			

and phonon thermal conductivity, respectively. Thus, maximizing ZT values is crucial for enhancing the performance of thermoelectric devices, driving research towards discovering and optimizing materials with superior thermoelectric properties [10].

Within the framework of the Boltzmann theory, both electrical conductivity and electronic thermal conductivity are contingent on the carrier relaxation time (τ), which in turn depends on the specific scattering mechanisms within the material. In this study, we consider the inherent electron scattering of selenium, where the primary interaction occurs with longitudinal acoustic phonons [70,71]. Within this theoretical framework, the relaxation time τ can be estimated using the following equation:

$$\tau = \frac{2(2\pi)^{1/2}\hbar^4 C}{3(k_B T m^*)^{3/2} E_1^2}, \tag{10}$$

where the constant strain potential (E_1), elastic modulus (C), and effective mass (m^*) have been considered. These parameters were accurately calculated and tabulated for selenium in Table IV. We validated our calculations by comparing them with reported theoretical [10] and experimental data [47], ensuring the reliability of our theoretical predictions.

The electronic thermal conductivity explored in this study is derived from the electrical conductivity, governed by the Wiedemann-Franz law,

$$k_e = LT\sigma \tag{11}$$

where the Lorenz number (L) is equal to 2.45×10^{-8} WΩ/K^2.

The lattice thermal conductivity as a function of temperature has been studied. Subsequently, based on these results, the Seebeck coefficient, electrical conductivity, and power factor will be analyzed concerning their n- and p-type contributions at room temperature, and for parallel and perpendicular directions to the c axis, and their polycrystalline average which is usually more interesting for potential applications. It has long been known that the thermoelectric properties of t-Se depend on whether they are measured or
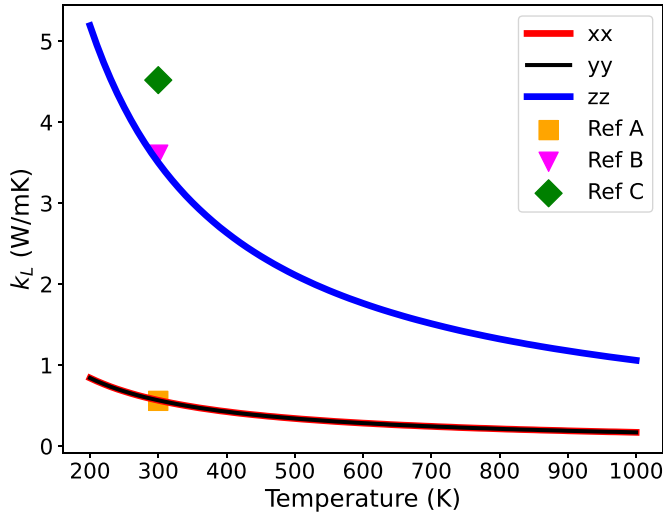
FIG. 4. Lattice thermal conductivity for selenium as a function of temperature along the x, y, and z directions. The yellow square and green diamond represent the experimental data for x/y and z directions from Ref A [72] and Ref B [73], respectively; and yellow square and purple triangle, the theoretical data for x/y and z directions from Ref C [10].

calculated parallel or perpendicular to the c axis [74]. Finally, ZT will be studied.

Figure 4 shows the lattice thermal conductivity (k_L) as a function of temperature in selenium. At room temperature, we found that k_L is 3.5 and 0.56 $\text{Wm}^{-1}\text{K}^{-1}$ in the z- and x/y-directions, respectively. These findings align with theoretical [10] and experimental measurements [72,73] in z- and x/y-directions, yielding values within the same order of magnitude as those reported in the literature. This congruence not only underscores the accuracy of our computational approach but also reinforces the validity of our results in the context of both experimental and theoretical observations. Additionally, as we explore the lattice thermal conductivity of selenium along the direction perpendicular to the chain, a striking feature emerges. In this orientation, the thermal conductivity exhibits an exceptionally low value, 6.25 times lower than that observed in the parallel direction. This distinctive anisotropic behavior is indicative of a clear quasi-one-dimensional heat transfer feature in selenium. The observed anisotropy in thermal conductivity is attributed to several contributing factors: the combination of small phonon group velocity, the mixing of acoustic-optical phonon branches, and bonding anharmonicity along the direction perpendicular to the chain collectively contribute to this high directional sensitivity in thermal transport.

Figure 5 illustrates $|S|$, σ, power factor, and ZT transport properties for p- (left side) and n-type (right side) doped selenium as a function of carrier concentration at 300 K. Calculations have been performed for parallel (z: green line) and perpendicular (x/y: blue line) directions to the c axis, and their average (Avg: red line) within the constant relaxation time approach, as implemented in BoltzTrap2 [75].

Figures 5(a) and 5(b) depict the absence of significant anisotropic behavior in the Seebeck coefficient of trigonal selenium. This can be attributed to several factors inherent to its crystal structure and electronic properties [10,51].
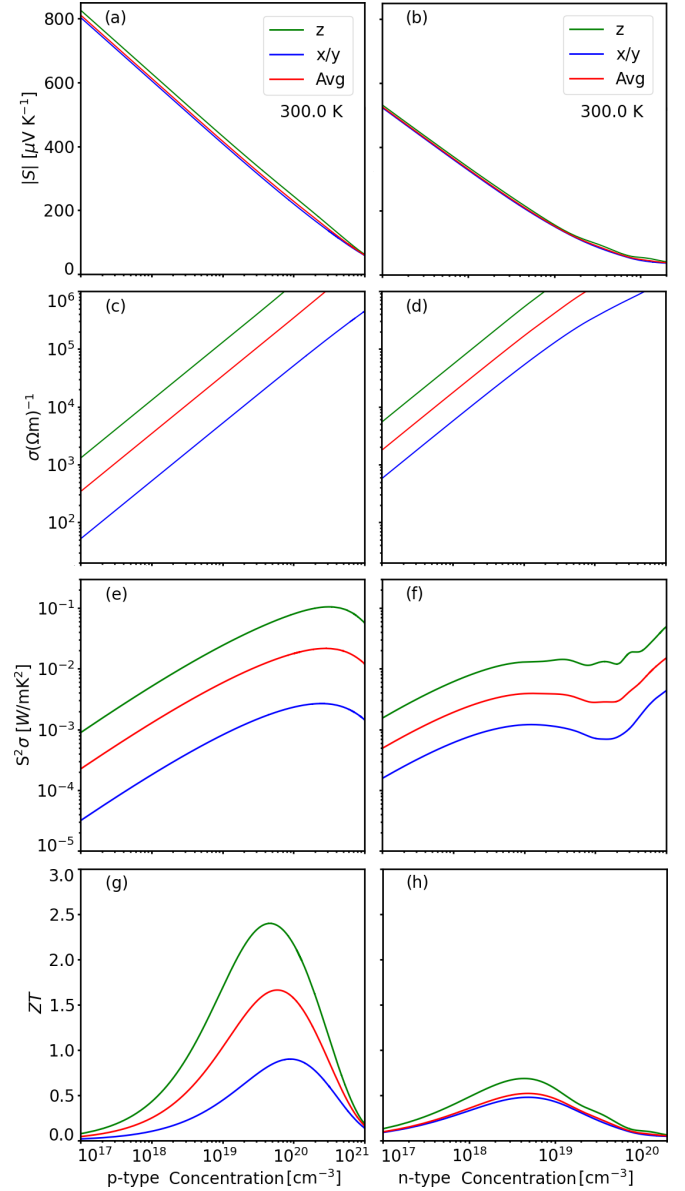

FIG. 5. Parallel (z: green line) and perpendicular (x: blue line) to the c axis electronic transport parameters, and their average (Avg: red line), for p- (left side) and n-type (right side) doped selenium as a function of carrier concentration at 300 K: (a) (b) Seebeck coefficient($|S|$), (c) (d) electrical conductivity (σ), (e) (f) power factor ($S^2\sigma$), and (g) (h) dimensionless figure of merit (ZT).

However, the value of the Seebeck coefficient of the p-type doped selenium is larger than that of n-type doping. This can be explained by the asymmetric differences between the band structures of holes and electrons, as shown in Fig. 3(a). This could favor the movement of holes over electrons in response to a temperature gradient.

Regarding electrical conductivity, Figs. 5(c) and 5(d) show that z-directional electrical conductivity is higher than -x/y for both p- and n-type, and it is superior for n-type. As shown in Table IV, the relaxation time for carriers (electrons or holes) in z- is higher than in x/y-direction. A longer relaxation time along the z axis suggests that electron (hole) motion is less scattered in that direction compared to the x/y directions,

TABLE V. $|S|$ (μVK^{-1}), σ (Ωm)$^{-1}$, power factor (W/mK^2) and ZT transport properties for p- and n-type doped selenium for parallel (z) and perpendicular (x/y) directions to the c axis at 300 K for the carrier concentration of 4.5×10^{19} cm^{-3}. Reference [10] has been used as comparison with a carrier concentration of 2.40×10^{19} cm^{-3}.

	Carrier	$|S|$	σ ($\times10^4$)	$S^2\sigma$ ($\times10^{-3}$)	ZT
Se$_{x/y}$	n-type	71.10	19.70	1.00	0.17
[10]				0.85	0.35
Se$_{x/y}$	p-type	284	2.18	1.75	0.82
[10]		250		2.50	0.60
Se$_z$	n-type	80.20	214	13.80	0.23
[10]				13.30	0.35
Se$_z$	p-type	308	59.2	56.1	2.43
[10]		275		60	2.70

increasing its conductivity in z axis. It implies that trigonal selenium exhibits an anisotropic nature, meaning its electrical conductivity varies with direction. On the other hand, the electrons have a lower effective mass compared to holes in selenium semiconductor material, as shown in Table IV. This lower effective mass allows electrons to respond more readily to an applied electric field, contributing to higher conductivity, as shown in Figs. 5(c) and 5(d).

The optimized relationship between the Seebeck coefficient and electrical conductivity can tailor material properties to enhance the power factor, thereby improving overall thermoelectric efficiency. From Figs. 5(a)–5(d), it can been seen that $|S|$ and σ follow opposing trends with carrier concentration. Thus, the power factor reaches its maximum value at the optimized carrier concentration.

To assess the figure of merit (ZT) value, we utilize our optimized lattice thermal conductivities of 3.5 W/mK (0.56 W/mK) in the z (x/y) direction, and their respective relaxation time τ for both p- and n-type carrier, as shown in Fig. 4 and Table IV, respectively. Our findings depict that the maximum value for ZT along z-and x/y-direction are 2.43 and 0.82 for a hole concentration of 4.5×10^{19} cm^{-3} at 300 K. Zhang *et al.* [10] reported that the maximum value for ZT along z-and x/y-direction are 2.70 and 0.60 for a hole concentration of 2.40×10^{19} cm^{-3} at 300 K. Our results show agreement with this study, as shown in Table V. Conversely, Peng *et al.* [51] observed that the maximum values for ZT along z-and x/y-direction are 0.63 and 0.24 for a hole concentration of 1.38×10^{20} cm^{-3} at 300 K. The main differences of the calculated ZT values lie on the methodology they used to find both the carrier relaxation time and ZT value, which does not include the effect of crystal anisotropy in the lattice thermal conductivity. Their relaxation time is determined using the formula $\tau = \text{ne}\mu/(\sigma/t)$, where μ represents experimentally observed hole mobility values of 26 cm^2/Vs and 7 cm^2/Vs, and $n = 1.38 \times 10^{20}$ cm^{-3}. The same mobility value is assumed for electrons and holes. Additionally, a room temperature lattice thermal conductivity of 0.52 W/mK is utilized to assess the ZT. In order to evaluate these results, we

use the same methodology as Peng *et al.* [51] and calculate the maximum value for ZT along z-and x/y-direction. Our results are 0.98 and 0.29, respectively, for a hole concentration of 1.38×10^{20} cm^{-3} at 300 K, which are of the same order as those found by Peng *et al.*

Peng *et al.* [76] noted that the Seebeck coefficients for both n- and p-type doped tellurium are notably high at room temperature. They reach a maximum value of 450 μV/K at a hole concentration of around 10^{17} cm^{-3}. The authors also highlight that these Seebeck values for a single-element solid are comparable to those reported for optimized Bi$_2$Te$_3$ [77]. Our Seebeck coefficients for both p- and n-type doped selenium at room temperature and a hole concentration of 10^{17} cm^{-3} are 818 and 531 μV/K, respectively. These values displays superiority when compared with t-Te.

The ZT value we obtained for t-Se is alike to that of SnSe [78] layered thermoelectric material. Our findings reveal that bulk selenium holds promise as a thermoelectric material by adjusting the carrier concentration accordingly.

IV. CONCLUSIONS

In this study, we have investigated the thermoelectric and spin transport properties of bulk selenium, a chiral crystal, employing first-principles calculations and symmetry analysis. Band structure calculations revealed the presence of Rashba splitting arising from spin-orbit coupling, a remarkable feature in materials lacking inversion symmetry. This finding highlights the potential for tailoring spin-dependent phenomena in chiral crystals. Indeed, we observed the emergence of the considerable signal of the intrinsic spin Hall effect (SHE) and current-induced spin polarization (CISP) in the Se chiral crystal, suggesting its suitability for spintronic applications, particularly in the context of spin manipulation and control.

Our results revealed the quasi-one-dimensional nature of thermal transport in selenium, uncovering significant anisotropy in lattice thermal conductivity, electrical conductivity, and power factor, notably lower in the perpendicular direction. The optimized relationship between the Seebeck coefficient and electrical conductivity tailors material properties to enhance the power factor, thereby improving overall thermoelectric efficiency for t-Se. Our findings depict that the maximum value for ZT along z-and x/y-direction are 2.43 and 0.82, respectively, for a hole concentration of 4.5×10^{19} cm^{-3} at 300 K, consistent with another theoretical study reported by Zhang *et al.* [10]. The emergence of the spin Hall effect and current-induced spin polarization in Se, together with their promising thermoelectric properties, proposes these materials for further experimental exploration and potential applications in advanced thermoelectronic and spintronic devices.

[1] S. D. Ganichev, M. Trushin, and J. Schliemann, Spin polarization by current, in *Spintronics Handbook, Second Edition: Spin Transport and Magnetism* (CRC Press, Boca Raton, FL, 2019), pp. 317–338.

[2] A. Roy *et al.*, Long-range current-induced spin accumulation in chiral crystals, npj Comput. Mater. **8**, 243 (2022).

[3] Y. Wolf, Y. Liu, J. Xiao, N. Park, and B. Yan, Unusual spin polarization in the chirality-induced spin selectivity, ACS Nano **16**, 18601 (2022).

[4] H. Shishido, R. Sakai, Y. Hosaka, and Y. Togawa, Detection of chirality-induced spin polarization over millimeters in polycrystalline bulk samples of chiral disilicides $NbSi_2$ and $TaSi_2$, Appl. Phys. Lett. **119**, 182403 (2021).

[5] S.-H. Yang, R. Naaman, Y. Paltiel, and S. S. Parkin, Chiral spintronics, Nat. Rev. Phys. **3**, 328 (2021).

[6] N. J. Ghimire, A. S. Botana, J. S. Jiang, J. Zhang, Y.-S. Chen, and J. F. Mitchell, Large anomalous Hall effect in the chiral-lattice antiferromagnet $CoNb_3S_6$, Nat. Commun. **9**, 3280 (2018).

[7] D. Waldeck, R. Naaman, and Y. Paltiel, The spin selectivity effect in chiral materials, APL Mater. **9**, 040902 (2021).

[8] S. Lin, W. Li, Z. Chen, J. Shen, B. Ge, and Y. Pei, Tellurium as a high-performance elemental thermoelectric, Nat. Commun. **7**, 10287 (2016).

[9] D. S. Sanchez, I. Belopolski, T. A. Cochran, X. Xu, J.-X. Yin, G. Chang, W. Xie, K. Manna, V. Süß, C.-Y. Huang *et al.*, Topological chiral crystals with helicoid-arc quantum states, Nature (London) **567**, 500 (2019).

[10] J. Zhang *et al.*, High thermoelectric performance achieved in bulk selenium with nanostructural building blocks, ACS Appl. Electron. Mater. **3**, 3824 (2021).

[11] D. Vanderbilt and J. Joannopoulos, Total energies in Se. I. The trigonal crystal, Phys. Rev. B **27**, 6296 (1983).

[12] T. Furukawa, Y. Shimokawa, K. Kobayashi, and T. Itou, Observation of current-induced bulk magnetization in elemental tellurium, Nat. Commun. **8**, 954 (2017).

[13] L. Salemi and P. M. Oppeneer, Theory of magnetic spin and orbital Hall and Nernst effects in bulk ferromagnets, Phys. Rev. B **106**, 024410 (2022).

[14] Y. Zhang, J. Železný, Y. Sun, J. Van Den Brink, and B. Yan, Spin Hall effect emerging from a noncollinear magnetic lattice without spin–orbit coupling, New J. Phys. **20**, 073028 (2018).

[15] Y. Zhang, Y. Sun, H. Yang, J. Zelezny, S. P. P. Parkin, C. Felser, and B. Yan, Strong anisotropic anomalous hall effect and spin Hall effect in the chiral antiferromagnetic compounds Mn_3X ($X =$ Ge, Sn, Ga, Ir, Rh, and Pt), Phys. Rev. B **95**, 075128 (2017).

[16] H. Henkels and J. Maczuk, Anisotropic resistivities of selenium crystals at high frequencies, Phys. Rev. **91**, 1562 (1953).

[17] P. Bammes, R. Klucker, E. Koch, and T. Tuomi, Anisotropy of the dielectric constants of trigonal selenium and tellurium between 3 and 30 eV, Phys. Status Solidi (B) **49**, 561 (1972).

[18] B. Geldiyev, M. Unzelmann, P. Eck, T. Kisslinger, J. Schusser, T. Figgemeier, P. Kagerer, N. Tezak, M. Krivenkov, A. Varykhalov, A. Fedorov, L. Nicolai, J. Minar, K. Miyamoto, T. Okuda, K. Shimada, D. DiSante, G. Sangiovanni, L. Hammer, M. A. Schneider *et al.*, Strongly anisotropic spin and orbital Rashba effect at a tellurium–noble metal interface, Phys. Rev. B **108**, L121107 (2023).

[19] J. K. Wrobel, R. Power, and M. Toborek, Biological activity of selenium: Revisited, IUBMB Life **68**, 97 (2016).

[20] Y. Huang, E. Su, J. Ren, and X. Qu, The recent biological applications of selenium-based nanomaterials, Nano Today **38**, 101205 (2021).

[21] C. M. Weekley and H. H. Harris, Which form is that? The importance of selenium speciation and metabolism in the prevention and treatment of disease, Chem. Soc. Rev. **42**, 8870 (2013).

[22] L. Jia, X. Sun, Y. Jiang, S. Yu, and C. Wang, A novel $MoSe_2$–reduced graphene oxide/polyimide composite film for applications in electrocatalysis and photoelectrocatalysis hydrogen evolution, Adv. Funct. Mater. **25**, 1814 (2015).

[23] H. Peng, D. Hou, and G. Chen, Quasi-one-dimensional thermal transport in trigonal selenium crystal, J. Phys.: Condens. Matter **33**, 455402 (2021).

[24] P. E. Blöchl, Projector augmented-wave method, Phys. Rev. B **50**, 17953 (1994).

[25] G. Kresse and D. Joubert, From ultrasoft pseudopotentials to the projector augmented-wave method, Phys. Rev. B **59**, 1758 (1999).

[26] G. Kresse and J. Furthmüller, Efficiency of *ab-initio* total energy calculations for metals and semiconductors using a plane-wave basis set, Comput. Mater. Sci. **6**, 15 (1996).

[27] G. Kresse and J. Furthmüller, Efficient iterative schemes for *ab initio* total-energy calculations using a plane-wave basis set, Phys. Rev. B **54**, 11169 (1996).

[28] P. Hohenberg and W. Kohn, Inhomogeneous electron gas, Phys. Rev. **136**, B864 (1964).

[29] W. Kohn and L. J. Sham, Self-consistent equations including exchange and correlation effects, Phys. Rev. **140**, A1133 (1965).

[30] J. P. Perdew, K. Burke, and M. Ernzerhof, Generalized gradient approximation made simple, Phys. Rev. Lett. **77**, 3865 (1996).

[31] S. Grimme, Semiempirical gga-type density functional constructed with a long-range dispersion correction, J. Comput. Chem. **27**, 1787 (2006).

[32] H. J. Monkhorst and J. D. Pack, Special points for Brillouin-zone integrations, Phys. Rev. B **13**, 5188 (1976).

[33] A. Togo, L. Chaput, T. Tadano, and I. Tanaka, Implementation strategies in phonopy and phono3py, J. Phys.: Condens. Matter **35**, 353001 (2023).

[34] A. Togo, First-principles phonon calculations with phonopy and phono3py, J. Phys. Soc. Jpn. **92**, 012001 (2023).

[35] G. K. Madsen and D. J. Singh, Boltztrap. a code for calculating band-structure dependent quantities, Comput. Phys. Commun. **175**, 67 (2006).

[36] A. A. Mostofi *et al.*, wannier90: A tool for obtaining maximally-localised Wannier functions, Comput. Phys. Commun. **178**, 685 (2008).

[37] J. Železný, Y. Zhang, C. Felser, and B. Yan, Spin-polarized current in noncollinear antiferromagnets, Phys. Rev. Lett. **119**, 187204 (2017).

[38] S. K. Barman, M. N. Huda, J. Asaadi, E. Gramellini, and D. Nygren, Surface and optoelectronic properties of ultrathin trigonal selenium: A density functional theory study with van der Waals correction, Langmuir **38**, 8485 (2022).

[39] D. McCann, L. Cartz, R. Schmunk, and Y. Harker, Compressibility of hexagonal selenium by x-ray and neutron diffraction, J. Appl. Phys. **43**, 1432 (1972).

[40] W. Teuchert, R. Geick, G. Landwehr, H. Wendel, and W. Weber, Lattice dynamics of trigonal selenium. I. Phonon spectra, J. Phys. C **8**, 3725 (1975).

[41] S. Yi, Z. Zhu, X. Cai, Y. Jia, and J.-H. Cho, The nature of bonding in bulk tellurium composed of one-dimensional helical chains, Inorg. Chem. **57**, 5083 (2018).

[42] R. Keller, W. Holzapfel, and H. Schulz, Effect of pressure on the atom positions in Se and Te, Phys. Rev. B **16**, 4404 (1977).

[43] M. Cheng, S. Wu, Z.-Z. Zhu, and G.-Y. Guo, Large second-harmonic generation and linear electro-optic effect in trigonal selenium and tellurium, Phys. Rev. B **100**, 035202 (2019).

[44] R. H. Asendorf, Space group of tellurium and selenium, J. Chem. Phys. **27**, 11 (1957).

[45] P. Cherin and P. Unger, The crystal structure of trigonal selenium, Inorg. Chem. **6**, 1589 (1967).

[46] G. H. Fecher, J. Kübler, and C. Felser, Chirality in the solid state: Chiral crystal structures in chiral and achiral space groups, Materials **15**, 5812 (2022).

[47] D. Royer and E. Dieulesaint, Elastic and piezoelectric constants of trigonal selenium and tellurium crystals, J. Appl. Phys. **50**, 4042 (1979).

[48] R. Nielsen *et al.*, Origin of photovoltaic losses in selenium solar cells with open-circuit voltages approaching 1 V, J. Mater. Chem. A **10**, 24199 (2022).

[49] H. Moustafa, J. Kangsabanik, F. Bertoldo, S. Manti, K. S. Thygesen, K. W. Jacobsen, and T. Olsen, Selenium and the role of defects for photovoltaic applications, Phys. Rev. Mater. **8**, 015402 (2024).

[50] M. Hirayama, R. Okugawa, S. Ishibashi, S. Murakami, and T. Miyake, Weyl node and spin texture in trigonal tellurium and selenium, Phys. Rev. Lett. **114**, 206401 (2015).

[51] H. Peng and G. Chen, Doping and biaxial deformation engineering the thermoelectric transport properties in selenium crystal, Solid State Commun. **297**, 34 (2019).

[52] S. Tutihasi and I. Chen, Optical properties and band structure of trigonal selenium, Phys. Rev. **158**, 623 (1967).

[53] I. Hadar, T.-B. Song, W. Ke, and M. G. Kanatzidis, Modern processing and insights on selenium solar cells: The world's first photovoltaic device, Adv. Energy Mater. **9**, 1802766 (2019).

[54] K. Wang, Y. Shi, H. Zhang, Y. Xing, Q. Donga, and T. Ma, Selenium as a photoabsorber for inorganic–organic hybrid solar cells, Phys. Chem. Chem. Phys. **16**, 23316 (2014).

[55] B. Moreth, Two types of indirect-exciton ground states in trigonal selenium, Phys. Rev. Lett. **42**, 264 (1979).

[56] H. Zetsche and R. Fischer, Photoluminescence of trigonal selenium single crystals, J. Phys. Chem. Solids **30**, 1425 (1969).

[57] R. Lundgren, P. Laurell, and G. A. Fiete, Thermoelectric properties of Weyl and dirac semimetals, Phys. Rev. B **90**, 165115 (2014).

[58] H. Xiang and D. J. Singh, Suppression of thermopower of Na_xCoO_2 by an external magnetic field: Boltzmann transport combined with spin-polarized density functional theory, Phys. Rev. B **76**, 195111 (2007).

[59] R. C. Andrew, R. E. Mapasha, A. M. Ukpong, and N. Chetty, Mechanical properties of graphene and boronitrene, Phys. Rev. B **85**, 125428 (2012).

[60] M. de Jong, W. Chen, T. Angsten *et al.*, Charting the complete elastic properties of inorganic crystalline compounds, Sci. Data **2**, 150009 (2015).

[61] R. M. Martin, *Electronic Structure: Basic Theory and Practical Methods* (Cambridge University Press, Cambridge, 2020).

[62] A. González-García, W. López-Pérez, and R. González-Hernández, Theoretical study of magnetic ordering and electronic properties of $Ag_xAl_{1-x}N$ compounds, Solid State Commun. **151**, 1794 (2011).

[63] E. D. Palik, *Handbook of Optical Constants of Solids*, Vol. 3 (Academic Press, New York, 1998).

[64] E. Ertekin, M. T. Winkler, D. Recht, A. J. Said, M. J. Aziz, T. Buonassisi, and J. C. Grossman, Insulator-to-metal transition in selenium-hyperdoped silicon: Observation and origin, Phys. Rev. Lett. **108**, 026401 (2012).

[65] M. Sakano, M. Hirayama, T. Takahashi, S. Akebi, M. Nakayama, K. Kuroda, K. Taguchi, T. Yoshikawa, K. Miyamoto, T. Okuda *et al.*, Radial spin texture in elemental tellurium with chiral crystal structure, Phys. Rev. Lett. **124**, 136404 (2020).

[66] A. Manchon, H. C. Koo, J. Nitta, S. M. Frolov, and R. A. Duine, New perspectives for Rashba spin–orbit coupling, Nat. Mater. **14**, 871 (2015).

[67] M. Seemann, D. Ködderitzsch, S. Wimmer, and H. Ebert, Symmetry-imposed shape of linear response tensors, Phys. Rev. B **92**, 155138 (2015).

[68] See Supplemental Material at http://link.aps.org/supplemental/10.1103/PhysRevMaterials.8.063601 for explores the achiral structure transition, chiral-dependent properties, band gap size's impact on transport properties, and the contribution of phonons to the figure of merit for trigonal Se bulk.

[69] G. J. Snyder and E. S. Toberer, Complex thermoelectric materials, Nat. Mater. **7**, 105 (2008).

[70] A. Mukherjee, D. Vasileska, and A. Goldan, Hole transport in selenium semiconductors using density functional theory and bulk Monte Carlo, J. Appl. Phys. **124**, 235102 (2018).

[71] J. Bardeen and W. Shockley, Deformation potentials and mobilities in non-polar crystals, Phys. Rev. **80**, 72 (1950).

[72] D. R. Lide, *CRC Handbook of Chemistry and Physics*, Vol. 85 (CRC Press, Boca Raton, FL, 2004).

[73] C. Y. Ho, R. W. Powell, and P. E. Liley, Thermal conductivity of the elements, J. Phys. Chem. Ref. Data **1**, 279 (1972).

[74] H. W. Henkels, Thermoelectric power and mobility of carriers in selenium, Phys. Rev. **77**, 734 (1950).

[75] G. K. Madsen, J. Carrete, and M. J. Verstraete, Boltztrap2, a program for interpolating band structures and calculating semiclassical transport coefficients, Comput. Phys. Commun. **231**, 140 (2018).

[76] H. Peng, N. Kioussis, and G. J. Snyder, Elemental tellurium as a chiral *p*-type thermoelectric material, Phys. Rev. B **89**, 195206 (2014).

[77] L. Goncalves, C. Couto, P. Alpuim, A. G. Rolo, F. Völklein, and J. H. Correia, Optimization of thermoelectric properties on Bi_2Te_3 thin films deposited by thermal co-evaporation, Thin Solid Films **518**, 2816 (2010).

[78] L.-D. Zhao, S.-H. Lo, Y. Zhang, H. Sun, G. Tan, C. Uher, C. Wolverton, V. P. Dravid, and M. G. Kanatzidis, Ultralow thermal conductivity and high thermoelectric figure of merit in SnSe crystals, Nature (London) **508**, 373 (2014).